

Superconductor-semiconductor hybrid cavity quantum electrodynamics

Guido Burkard¹, Michael J. Gullans², Xiao Mi^{2,*}, and Jason R. Petta²

1. Department of Physics, University of Konstanz, D-78457 Konstanz, Germany

2. Department of Physics, Princeton University, Princeton, New Jersey 08544, USA

* Present address: Google Inc., Santa Barbara, California 93117, USA

Abstract | Light-matter interactions at the single particle level have generally been explored in the context of atomic, molecular, and optical physics. Recent advances motivated by quantum information science have made it possible to explore coherent interactions between photons trapped in superconducting cavities and superconducting qubits. Spins in semiconductors can have exceptionally long spin coherence times and can be isolated in silicon, the workhorse material of the semiconductor microelectronic industry. Here, we review recent advances in hybrid “super-semi” quantum systems that coherently couple superconducting cavities to semiconductor quantum dots. We first present an overview of the underlying physics that governs the behavior of superconducting cavities, semiconductor quantum dots, and their modes of interaction. We then survey experimental progress in the field, focusing on recent demonstrations of cavity quantum electrodynamics in the strong coupling regime with a single charge and a single spin. Finally, we broadly discuss promising avenues of future research.

A remarkable experimental achievement of the 1980’s and 1990’s was to create minimalistic hybrid systems consisting of only one single atom, which exists in one of two states, and interacts with individual photons in a cavity¹⁻⁴. This field of research, termed cavity QED, showed that it is possible to create a quantum superposition of light and matter⁵. More complex systems such as superconductors and semiconductors can themselves be building blocks in hybrid systems on a larger scale. In the early 2000’s, cavity QED was realized in condensed matter systems using self-assembled quantum dots confined in photonic cavities⁶⁻⁸ and by placing a superconducting qubit inside of a microwave cavity^{9, 10}. In these experiments the atom that is conventionally used in atomic cavity QED is replaced with a quantum device that has discrete energy levels whose energy separation can be matched to the energy of a cavity photon. Around the same time, it was conjectured that cavity QED could be performed using individual electrons trapped in gate defined semiconductor quantum dots, using either charge or spin degrees of freedom to mimic the states of an atom¹¹⁻¹³.

There are a number of motivations for examining cavity QED in the context of condensed matter systems, many of which are grounded in the rapidly growing field of quantum information science. On the heels of the discovery that a superconducting circuit could be coherently coupled to microwave photons¹⁰ were two experiments showing that two spatially separated superconducting qubits could be coupled via a cavity^{14, 15}. The then nascent subject of circuit QED has now expanded into a field of its own. Prominent advances include demonstrations of multiqubit entanglement¹⁶⁻¹⁹, readout of quantum states²⁰⁻²², the generation of non-classical light²³⁻²⁵, the development of error correction based on Schrodinger cat states^{26, 27}, quantum feedback^{28, 29} and measurements of quantum trajectories³⁰. Fundamentally, experiments involving superconducting quantum devices take advantage of a macroscopic superconducting condensate that is protected by an energy gap Δ (e.g. $\Delta \sim 175 \mu\text{eV}$ in Al, roughly 20 times larger than the thermal energy $100 \text{ mK} \sim 8 \mu\text{eV}$ in typical experiments). This begs the question: can cavity QED physics be explored with single charges and spins in semiconductor devices, where

such protection is absent? The prospect of cavity QED with a single spin is especially intriguing, as spin coherence times can exceed seconds in some solid state systems³¹⁻³³.

In this Review, we describe dramatic developments in the area of “hybrid” circuit QED, where gate defined quantum dots are coupled to superconducting cavities in a “super-semi” device architecture. Recent demonstrations of strong coupling physics with single charges and spins confined in semiconductor quantum dots make this a timely topic to review³⁴⁻³⁸. We begin by laying the theoretical groundwork for the experiments, with a description of the superconducting cavity, the “artificial atom” which in most experiments consists of a semiconductor double quantum dot (DQD), their modes of interaction, and the figures of merit that succinctly describe the quantum coherence of the system. We then survey experiments involving the charge degree of freedom, which interacts with the cavity electric field through the electric dipole interaction^{34, 35}. A combination of electric dipole coupling and spin-orbit coupling enables coherent spin-photon interactions, which we review next^{36, 37}. Lastly, we give several examples illustrating how semiconductor circuit QED could impact fundamental science and engineering in diverse areas ranging from topological physics to surface microscopy and quantum technology.

1. Cavity QED with double quantum dots

At a basic level, a typical cavity QED system (FIG 1a) consists of just two components: a cavity that supports a well-defined photon mode at a cavity resonance frequency f_c , and a two-level quantum system with a transition energy $E_{|1\rangle} - E_{|0\rangle}$ that is closely matched to the energy of a photon trapped in the cavity hf_c , where h is Planck’s constant. Here $E_{|0\rangle}$ ($E_{|1\rangle}$) is the ground state (first excited state) energy. The first atomic physics demonstrations of cavity QED used microwave transitions between Rydberg states of single cesium atoms^{39, 40}. These results were eventually extended to the visible spectral range⁴¹. Cavity QED can also be implemented using a wide variety of solid-state systems, as illustrated with some examples in FIG 1b. Color centers in diamond such as nitrogen vacancy (NV) centers have spin-full ground states and narrow, spin-selective microwave and optical transitions, which allows the realization of cavity QED using integrated photonic structures⁴²⁻⁴⁶. Using nanofabrication techniques, it is possible to build mesoscopic semiconducting and superconducting devices that are quantum coherent.

Semiconductor DQDs can be used to isolate single electrons, where the charge degree of freedom can be controlled with electric fields⁴⁷⁻⁴⁹ and the spin degree of freedom with magnetic fields⁵⁰ and the exchange interaction⁵¹. Superconducting circuits combine a capacitance C with a Josephson inductance L_J to create a quantum system with an anharmonic energy level spectrum⁵²⁻⁵⁷. Cavity QED experiments involving superconducting quantum devices are reviewed in REFS^{58, 59}. We focus here on experiments involving semiconductor DQDs^{60, 61}, as they are electrically tunable and open the door to cavity QED using long-lived spin states (see FIG 2a).

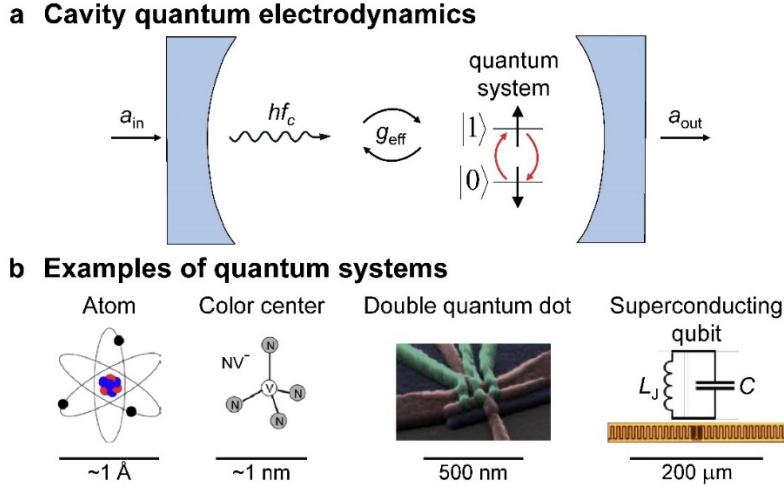


Figure 1 | **Cavity quantum electrodynamics.** **a** | Cavity quantum electrodynamics (cavity QED) explores the interaction between light and matter at the single particle level. In general, a quantum system with excited (ground) state energy $E_{|1\rangle}$ ($E_{|0\rangle}$) is placed inside of a high quality factor cavity that traps photons of energy hf_c . Cavity losses are described by a cavity decay rate κ (not shown). The quantum system interacts with the electromagnetic field of the cavity and the interaction is characterized by a coupling frequency g_{eff} . In the dispersive regime, $E_{|1\rangle} - E_{|0\rangle} - hf_c \gg \hbar g_{\text{eff}}$, and the quantum system weakly interacts with the cavity field. Readout can be performed in the dispersive regime by driving the cavity with a weak input field a_{in} and measuring the transmission through the cavity $a_{\text{out}}/a_{\text{in}}$. In the resonant regime, $E_{|1\rangle} - E_{|0\rangle} \approx hf_c$. Here the quantum system hybridizes with the photonic mode, forming a superposition state of light and matter. **b** Cavity QED has been implemented with many different quantum systems. Early work in atomic physics focused on atoms, but the field has branched out to include color centers, semiconductor DQDs, and superconducting qubits.

Box 1: Double quantum dot

A quantum dot (QD) is a nanoscale object that confines an electron in all three spatial dimensions⁶⁰⁻⁶². Single quantum dots are described by the electrostatic charging energy $E_c = e^2/2C$, which is the energy cost to add or remove an electron from the system. Here $C \approx 4\pi\epsilon_r\epsilon_0 a_0$ denotes the capacitance of the QD and e the elementary charge of an electron, where ϵ_r is the (relative) dielectric constant, ϵ_0 is the permittivity of free space, and a_0 is the radius of the quantum dot. The orbital “particle-in-a-box” energy scale is governed by $E_{\text{orb}} \sim \hbar^2/m^* a_0^2$, where $\hbar = h/2\pi$ is the reduced Planck constant and m^* is the effective mass of the electron. Both of these energy scales are set by the physical dimensions of the dot (a_0) and materials parameters (m^* and ϵ_r), and are therefore difficult to change in-situ. Fortunately, it is possible to make an artificial molecule by placing two quantum dots in proximity to each other and forming a DQD. In semiconductor DQDs, the energy level separation ϵ and the interdot tunneling rate t_c can be electrically tuned (FIG 2a).

A DQD containing a single electron can be viewed as a charge qubit; a voltage-tunable double well potential containing a single charge, as illustrated in FIG 2b^{47-49, 63}. The charge physics of a DQD is described by the Hamiltonian

$$H_0 = \begin{pmatrix} \varepsilon/2 & t_c \\ t_c & -\varepsilon/2 \end{pmatrix}$$

which is written in the basis $|L\rangle = |(1,0)\rangle$, $|R\rangle = |(0,1)\rangle$, where $|(N_L, N_R)\rangle$ denotes a DQD charge state with N_L (N_R) electrons occupying the left (right) dot⁴⁷⁻⁴⁹. In other words, $|L\rangle$ and $|R\rangle$ describe two charge states where the electron is in the left or right dot, respectively. If the left and right dot energy levels are aligned ($\varepsilon=0$) then the $|L\rangle$ and $|R\rangle$ states hybridize to form molecular bonding and antibonding states $|\pm\rangle \propto |L\rangle \pm |R\rangle$, while at large detuning ($|\varepsilon| \gg t_c$) the states $|L\rangle$ and $|R\rangle$ are essentially unperturbed by tunneling. The energy of the two levels is plotted as a function of level detuning ε in FIG 2c. The states $|+\rangle$ and $|-\rangle$ allow for electric dipole transitions around $\varepsilon \approx 0$ and play the role of the atomic levels for cavity QED¹. To take into account the fact that an electron is endowed with a spin- $1/2$ degree of freedom, we extend our basis to $|(\uparrow, 0)\rangle$, $|(\downarrow, 0)\rangle$, $|(0, \uparrow)\rangle$, $|(0, \downarrow)\rangle$, where the arrow indicates the spin state of the electron⁶⁴.

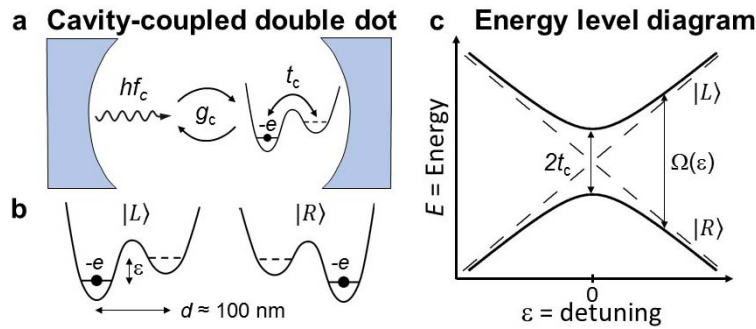


Figure 2 | Physics of the cavity-coupled double quantum dot. a | Electric dipole interactions couple a single electron trapped in the DQD to single cavity photon with a strength described by the charge-photon coupling rate g_c . **b** The two charge states of the DQD, $|L\rangle$ or $|R\rangle$, are defined by the presence of one electron on the left or right dot, respectively. The interdot spacing is typically on the order of $d = 100$ nm, which leads to a substantial electric dipole moment. **c** Energy level diagram of the DQD charge states. Both ε and t_c are electrically tunable with gate voltages. As the detuning parameter is increased from zero, the effective dipole moment is reduced by a factor $\frac{2t_c}{\Omega(\varepsilon)}$, where $\Omega = E_{|L\rangle} - E_{|R\rangle} = \sqrt{\varepsilon^2 + 4t_c^2}$ and becomes negligible for large detunings.

Charge-photon interaction

A single electron trapped in a DQD forms a fully tunable two-level system (see Box 1). The basic physics of charge-photon coupling in a DQD system is illustrated in FIG. 2a. Electric dipole interactions couple the electron trapped in the DQD to the cavity photon with a strength

described by the charge-photon coupling rate g_c . The interdot spacing is typically on the order of $d = 100$ nm, which leads to an electric dipole moment ed that is about 1000x larger than the dipole moment of a single atom. The coupling rate g_c is given by the product of this dipole moment with the vacuum (rms) electric field E_0 of the cavity. Near zero detuning ($\varepsilon=0$) the charge states are strongly hybridized, leading to the maximum in the charge-photon coupling rate. Away from zero detuning, the $|L\rangle$ - $|R\rangle$ charge states are weakly admixed, which reduces the effective dipole moment by a factor $\frac{2t_c}{\Omega(\varepsilon)}$, where $\Omega(\varepsilon) = E_{|L\rangle} - E_{|R\rangle} = \sqrt{\varepsilon^2 + 4t_c^2}$.

Fabry-Perot cavities are typically employed in atomic physics, where optical photons are trapped⁴¹. For the much larger quantum dot devices, typical energy scales are on the order of 20-40 μeV and it becomes convenient to use superconducting resonators to trap microwave frequency photons (1 GHz \sim 4.2 μeV). A cavity is never perfect and there can be internal losses, described by a decay rate κ_{int} , and losses through the ports of the cavity, κ_1 and κ_2 . Cavity QED systems can be probed by measuring the transmission through (or reflection off of) the cavity. For example, in FIG 1a, port 1 is being driven by a weak input field a_{in} and the signal exiting port 2 of the cavity a_{out} is being measured.

When a DQD is placed inside a superconducting microwave resonator, the electric field E_{res} inside the resonator tilts the energy landscape and the difference ε between the left and right energy levels becomes $\varepsilon + eE_{\text{res}}d$. Here, since d is much smaller than the wavelength of the electromagnetic waves inside the resonator, we can apply the electric dipole approximation where E_{res} is constant within the entire volume of the DQD. The quantized electric field operator can be expressed in terms of creation and annihilation operators a and a^\dagger of the electromagnetic field mode inside the resonator (these are equivalent to the ladder operators of the quantum harmonic oscillator), as $E_{\text{res}} = E_0(a + a^\dagger)$ where E_0 is the vacuum amplitude of the electric field. Taken together, the coupling of the charge qubit to the resonator mode is described with the Hamiltonian $H = H_0 + H_{\text{int}}$ with $H_{\text{int}} = g_c(a + a^\dagger)\tau_z$ in units where $\hbar=1$, with the charge-cavity coupling $g_c = eE_0d$ and the quantum operator τ_z defined via $\tau_z|(1,0)\rangle = |(1,0)\rangle$ and $\tau_z|(0,1)\rangle = -|(0,1)\rangle$. The electric dipole $ed\tau_z$ of the DQD with one electron can be probed via microwave transmission through the cavity. Theoretically, this means that the DQD and cavity need to be treated as an open quantum system. The transmission can be efficiently calculated using input-output theory (see Box 2). It is advantageous to first diagonalize H_0 and transform H_{int} into the eigenbasis of H_0 . Transforming into a frame rotating with the probe field frequency and neglecting fast oscillating terms within the rotating-wave approximation, one finds $H = \frac{\Omega}{2}\tau_z + \tilde{g}_c(a\tau_+ + a^\dagger\tau_-) + \Delta a^\dagger a$ where $\tilde{g}_c = \frac{g_0 t_c}{\Omega}$, and where we have added the photon energy in the rotating frame $\Delta/2\pi = f_c - f_R$ with the probe frequency f_R (often $f_c = f_R$ and thus $\Delta = 0$). Here, the τ operators are defined in the eigenbasis of H_0 . The Heisenberg-Langevin equations of motion for the photon operator and the electron coherence operator are then found to be (see Box 2)

$$\dot{a} = -i\Delta a - \frac{\kappa}{2}a + \sum_n \sqrt{\kappa_n} a_{n,\text{in}}(t) - i\tilde{g}_c\tau_-,$$

$$\text{and } \dot{\tau}_- = -i\Omega\tau_- - \frac{\gamma}{2}\tau_- - i\tilde{g}_c a,$$

where we have neglected quantum noise terms⁶⁵⁻⁶⁷. Here, in addition to the coherent contributions from the quantum Heisenberg equations of motion, the incoherent terms take into account the cavity decay with rate $\kappa = \kappa_1 + \kappa_2 + \kappa_{\text{int}}$ (photon loss at the two ports plus intrinsic losses), the charge qubit decay rate γ , and the cavity input field $a_{n,\text{in}}$ on mirror n . In the stationary limit $\dot{a} = \dot{\tau}_- = 0$ we find for the transmission coefficient through the cavity

$$A = \frac{a_{2,\text{out}}}{a_{1,\text{in}}} = \frac{\sqrt{\kappa_2} a}{a_{1,\text{in}}} = \frac{-i\sqrt{\kappa_1\kappa_2}}{\Delta - \frac{i\kappa}{2} + \tilde{g}_c\chi},$$

with the single-electron electric susceptibility

$$\chi = \frac{\tilde{g}_c}{-\Omega + i\gamma/2}.$$

For simplicity, we can consider a symmetric cavity without intrinsic losses (e.g. $\kappa_{\text{int}} = 0$), such that $\kappa_1 = \kappa_2 = \kappa/2$. The cavity is also often probed on resonance ($\Delta = 0$). In the absence of a DQD, $\chi = 0$ and we find unhindered transmission of microwaves through the cavity ($A = 1$). Charge dynamics within the DQD results in an effective microwave admittance that loads the superconducting cavity, changing the cavity amplitude and phase response⁶⁸⁻⁷². The electric susceptibility χ is greatest (and thus A is the smallest) for a symmetric DQD ($\varepsilon = 0$) because in this configuration the electron is most easily transferred from left to right and back.

Box 2: Input-output theory primer

The cavity-DQD system can be accurately described using techniques from the theory of open quantum systems⁷³. In this formulation we break up the total Hamiltonian $H = H_s + H_r + V_{sr}$ into a system Hamiltonian H_s for the DQD, its surrounding environment, and a single mode of the cavity with bosonic operator a , a reservoir Hamiltonian H_r describing a bath of electromagnetic modes $b_n(f)$ for each port (“mirror”) coupled to the cavity mode, and an interaction Hamiltonian V_{sr} that couples the cavity mode to the reservoir

$$V_{sr} = \hbar \sum_n \int df \lambda_n(f) [b_n(f) a^\dagger + a b_n^\dagger(f)].$$

Under the condition that the coupling constants $\lambda_n(f)$ are approximately independent of the frequency f over the frequency range of interest, we can treat the reservoir as a Markovian bath. Formally integrating the Heisenberg equation of motion for $b_n(f, t)$ starting from an initial time $t_0 < t$, we arrive at closed Heisenberg equations of motion for $a(t)$

$$\dot{a}(t) = \frac{i}{\hbar} [H_s, a] - \frac{\kappa}{2} a(t) + \sum_n \sqrt{\kappa_n} a_{n,\text{in}}(t),$$

$$a_{n,\text{in}}(t) = \sqrt{2\pi} \int df b_n(f, t_0) e^{-2\pi i f(t-t_0)},$$

where $\kappa = \kappa_{\text{int}} + \sum_n \kappa_n$ is the total cavity decay rate including intrinsic loss κ_{int} , $\kappa_n = 2\pi|\lambda_n(f)|^2$ is the decay rate through port n of the cavity, and $a_{n,\text{in}}(t)$ is the “input” field incident on port n of the cavity. Applying a boundary condition on $b_n(f, t)$ at $t_1 > t$ gives rise to a similar equation for $a(t)$ in terms of “output” fields $a_{n,\text{out}}(t)$. The input and output fields have the simple relation

$$a_{n,\text{out}}(t) = \sqrt{\kappa_n} a(t) - a_{n,\text{in}}(t),$$

which allows for a complete description of the cavity response. In the main text we consider a two-port system with an input field on port 1 and $a_{2,\text{in}}(t) = 0$. The measured transmission coefficient A is then given by the ratio of the output field on port 2 $a_{2,\text{out}}(t) = \sqrt{\kappa_2} a(t)$ to the input field on port 1 $a_{1,\text{in}}(t)$.

Quantum coherent charge-photon coupling

The scale of the susceptibility $\chi \propto g_c$ and transmission $A \propto 1/g_c^2$ (assuming $\kappa \ll g_c$ and $\varepsilon = 0$ in the case of a DQD) are both determined by the electric dipole ed and the vacuum cavity electric field E_0 via the electron-dipole coupling strength $g_c = eE_0d$. For a Rydberg atom in an optical cavity, one has $E_0 \approx \text{mV/m}$ and $d \approx 100 \text{ nm}$, leading to couplings g_c roughly in the 10 or 100 kHz range⁷⁴. This coupling can in principle be strengthened in two ways: either by increasing the electric dipole through an increase in size or by increasing the vacuum electric field $E_0 = \sqrt{\hbar f_c / 2\epsilon_0 V}$, where f_c denotes the cavity frequency and V the cavity mode volume. While superconducting circuit microwave resonators typically have a slightly lower resonance frequency than three-dimensional cavities for Rydberg atom-based cavity QED, their mode volume can be thousands of times smaller than that of 3D cavities^{9, 10}. The vacuum electric field can therefore be several orders of magnitude stronger in superconducting resonators, which allows for qubit-resonator couplings of $g_c/2\pi \approx 1 - 10 \text{ MHz}$ for quantum dots ($d \approx 100 \text{ nm}$) and $g_c/2\pi \approx 10 - 100 \text{ MHz}$ for superconducting qubits ($d \approx 1 \mu\text{m}$). Crucially, such large values of g_c can easily exceed both the cavity linewidth κ and qubit decay rate γ . The limit $g_c \gg \gamma, \kappa$ is called the strong coupling regime of cavity QED. Achieving strong coupling is significant because the qubit and photon degrees of freedom become directly entangled with each other under these conditions⁷⁵. In addition to being of fundamental interest, this entanglement can be exploited for applications in quantum information science⁷⁶.

2. Experimental demonstrations of charge-photon coupling with quantum dots

Hybrid quantum devices comprising gate-defined quantum dots (QDs) that are coupled via their electric dipole moment to microwave cavities have been successfully demonstrated using multiple material systems including GaAs/AlGaAs heterostructures^{35, 77-80}, InAs nanowires^{67, 81}, graphene^{82, 83}, carbon nanotubes^{84, 85} and Si/SiGe heterostructures^{34, 36, 37, 86}. The microwave cavity is often realized as a superconducting coplanar waveguide resonator^{9, 10, 14, 24, 87}, with an example shown in the top left panel of FIG. 3a. In order to maximize the quality factor of the cavity and the chance of reaching the strong-coupling regime, each gate line leading to the DQD is sometimes filtered by an on-chip low pass LC-filter to suppress photon leakage from the cavity⁸⁶.

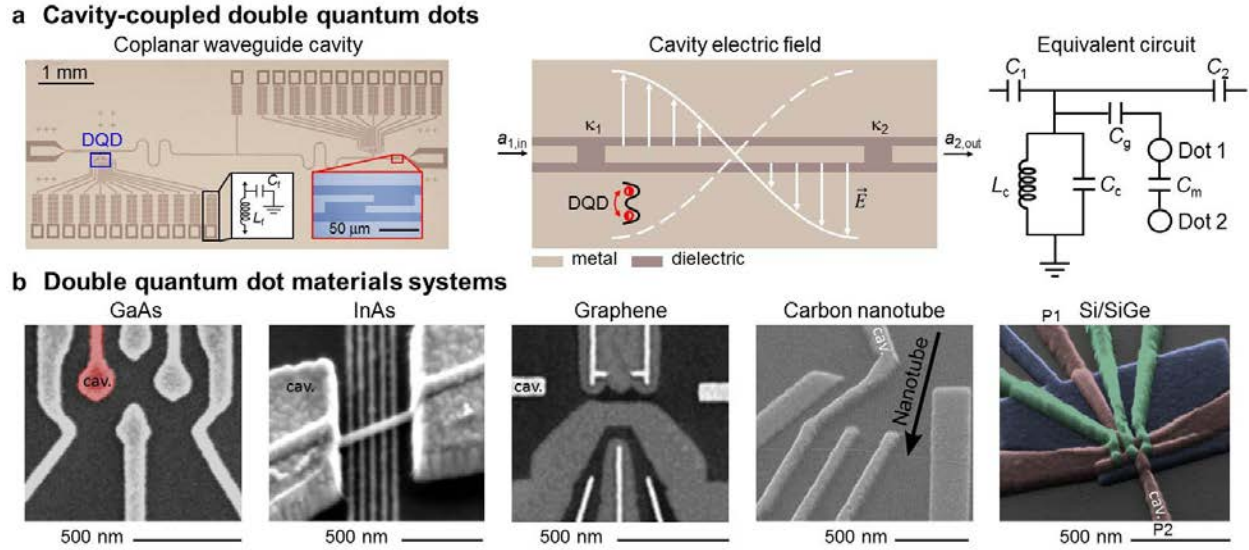


Figure 3 | Constructing cavity-coupled double quantum dots. **a** | Left panel: Optical image of a Nb coplanar waveguide cavity fabricated on top of a Si/SiGe heterostructure (adapted with permission from REF.³⁴, AAAS). The coplanar waveguide cavity is located in the middle of the sample and is coupled to measurement ports through vacuum gap capacitors located at each end of the cavity (see right inset). A gate-defined DQD is positioned at an anti-node of the cavity electric field. Low-pass LC-filters, as represented by the circuit diagram in the left inset, allow for dc biasing of the DQD gate electrodes and reduce photon losses from the cavity. Middle panel: Schematic representation of the device. A half-wavelength ($\lambda/2$) standing wave is formed in the coplanar waveguide cavity (white lines) and couples to a single electron trapped in the DQD via the electric-dipole interaction. In a typical experiment, port 1 of the cavity is driven by a coherent microwave field $a_{1,in}$ and the signal exiting port 2 of the cavity $a_{2,out}$ is measured. κ_1 (κ_2) denotes the coupling rate between the cavity and port 1 (port 2). Right panel: Circuit representation of the device. Here the microwave cavity is modeled as a parallel LC-oscillator with an effective inductance L_c and capacitance C_c . The DQD is modeled as a pair of charge islands with a mutual capacitance C_m and dot 1 is coupled to the LC-oscillator through a capacitance C_g . κ_1 (κ_2) is set by the port capacitance C_1 (C_2). **b** | Scanning electron micrographs of cavity-coupled DQDs fabricated from a variety of host materials, including GaAs (adapted with permission from REF.⁸⁸), InAs (adapted with permission from REF.⁸⁹, American Physical Society), graphene (adapted with permission from REF.⁸³, American Chemical Society), carbon nanotubes (adapted with permission from REF.⁹⁰, American Institute of Physics) and Si/SiGe (adapted with permission from REF.³⁴, AAAS). The gate electrode connected to the microwave cavity is indicated for each device by the letters “cav.”. The gates labeled V_{P1} (left dot) and V_{P2} (right dot) in the Si/SiGe device are used to adjust the DQD level detuning ε .

A simplified schematic of the hybrid device is depicted in the top middle panel of FIG. 3a. At the fundamental resonance frequency f_c , the vacuum fluctuation of the cavity generates a half-wavelength $\lambda/2$ electromagnetic standing wave^{10,91}. At a voltage anti-node of the standing wave,

a delocalized electron occupying the molecular bonding and anti-bonding states of the DQD^{47, 48, 60} couples to the electric field of the cavity via the electric-dipole interaction^{67, 77}. A circuit representation of the device is shown in the right panel of FIG. 3a. Here the cavity is modeled as a parallel LC -oscillator having an effective inductance L_c , effective capacitance C_c and resonance frequency $f_c = \sqrt{1/L_c C_c}/2\pi$ (REFS^{92, 93}). The DQD is mutually coupled via a capacitance C_m and dot 2 is capacitively coupled to the cavity via C_g . The system is connected to an input port via capacitor C_1 and an output port via capacitor C_2 , allowing for measurements of the cavity transmission amplitude $A = |a_{2,out}/a_{1,in}|$ and phase $\phi = -\arg(a_{2,out}/a_{1,in})$ using homodyne or heterodyne detection techniques^{10, 20, 94}.

Since the charge-photon coupling rate g_c scales linearly with $\sqrt{Z_c}$, where $Z_c = \sqrt{L_c/C_c}$ is the characteristic impedance of the cavity^{9, 55}, it is desirable to increase Z_c beyond the range between 20Ω and 200Ω that is the typical limit of co-planar waveguide cavities⁹³. One way of increasing the impedance is to define the microwave cavity using a linear array of superconducting quantum interference devices (SQUIDs) made from Al Josephson junctions, leading to $L_c \approx 1.5 \text{ k}\Omega$ by virtue of the large Josephson inductance of each SQUID³⁵. Another approach, discussed in the next section, utilizes the large kinetic inductance of a nanowire made from NbTiN^{37, 95}.

Detailed scanning electron micrographs (SEMs) of cavity-coupled DQDs made with different host materials are shown in FIG. 3b. In the case of GaAs or Si, one or three layers of surface gate electrodes are directly patterned on top of the buried quantum well (QW) of a GaAs/AlGaAs or Si/SiGe heterostructure^{77, 86}. For InAs nanowires, graphene and carbon nanotubes, the host material is first transferred to a Si substrate before the patterning of gate electrodes^{67, 82, 90}. To maximize g_c , an electrode is often galvanically connected to the center pin of the superconducting cavity^{34, 67, 77, 78, 82}.

Strong charge-photon coupling

Achieving the strong-coupling regime for DQD charge qubits is generally challenging due to their typically large decoherence rates γ_c , which commonly fall between a few hundred MHz and several GHz in earlier works^{47, 49, 63, 67, 77-79, 82, 85, 96, 97}. These values often exceed the coherent charge-photon coupling rate g_c by one or more orders of magnitude^{67, 77-80, 82, 85, 96, 97}. Therefore, a significant reduction in γ_c or a significant increase in g_c is needed to access the strong-coupling regime $g_c > (\gamma_c, \kappa)$. Both approaches have recently been met with success in two experiments which we review here^{34, 35}.

A first step toward charge-photon coupling is the detection of charge states within the DQD. This is traditionally accomplished by measuring the conductance of a proximal quantum point contact (QPC) which is sensitive to the charge distribution within the QDs⁹⁸⁻¹⁰⁰. Charge state detection may also be performed by measuring the transmission properties of the cavity, which are sensitive to the tunnel-rate-dependent complex admittance of the QDs^{68, 69, 72}. An example is shown in the upper panel of FIG. 4a. Here the cavity transmission amplitude A/A_0 (A_0 is a normalization constant) at a fixed drive frequency $f = f_c$ is measured as a function of gate voltages V_L and V_R (e.g., see right-most bottom panel of FIG. 3b), which control the chemical

potentials of the left and right dot, respectively. The charge stability diagram characteristic of a few-electron DQD is clearly visible⁶⁰, where we have used (N_L, N_R) to denote a charge state with N_L electrons in the left dot and N_R electrons in the right dot. To determine g_c , A/A_0 is measured around an interdot charge transition $(N_L+1, N_R)-(N_L, N_R+1)$ (bottom panel of FIG. 4a, taken with $2t_c/h < f_c$)⁶⁰. Here a pair of minima are observed along the DQD detuning axis ε at locations where $\Omega/h = f_c$. At these detunings the charge qubit is strongly hybridized with the cavity photons^{34, 67, 77}. Detailed fitting of the response $A(\varepsilon)/A_0$ to input-output theory allows the charge-photon coupling rate g_c to be extracted from this measurement^{34, 67, 77}.

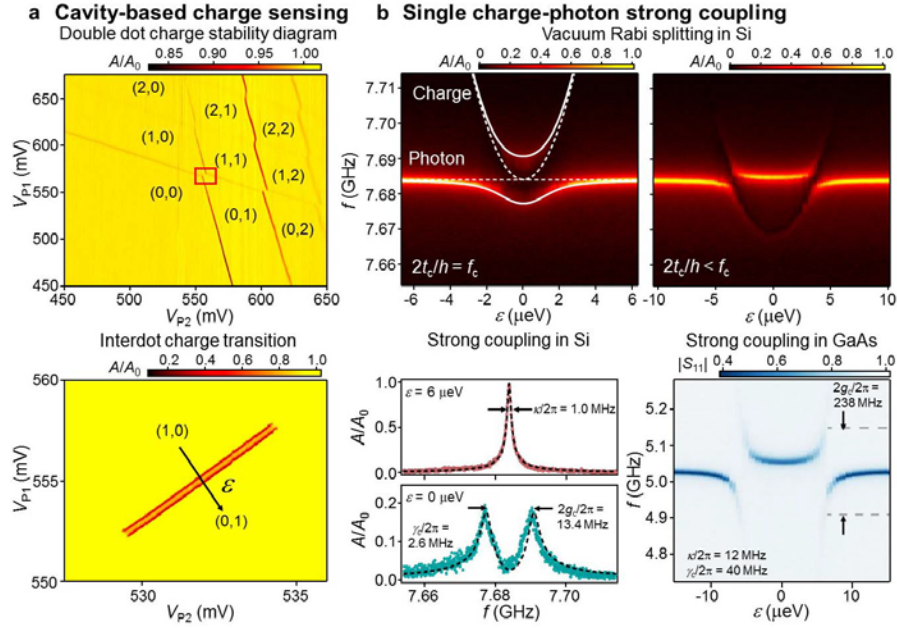


Figure 4 | Strong charge-photon coupling. a | Upper panel: The charge stability diagram of the DQD can be extracted by measuring the cavity transmission amplitude A/A_0 as a function of the left and right gate voltages. Dot-lead transitions correspond to the exchange of an electron between the source/drain reservoirs and the DQD. Interdot charge transitions correspond to the transfer of an electron between dots and are also visible in the data. Bottom panel: Cavity transmission amplitude A/A_0 measured in the vicinity of the $(1,0)-(0,1)$ interdot transition of the same device after the interdot tunnel coupling t_c has been increased. The arrow denotes the axis along which the DQD level detuning parameter ε is defined. **b** | Top panels: Cavity transmission amplitude A/A_0 of a Si-based device as a function of ε and the drive frequency f , taken with $2t_c/h = f_c$ (top left panel) and $2t_c/h < f_c$ (top right panel). The white solid (dashed) lines indicate the eigenenergies of the Jaynes-Cummings Hamiltonian describing the charge-photon system, when $g_c/2\pi = 6.7$ MHz (0 MHz). Bottom left panels: A/A_0 as a function of f when $\varepsilon = 6 \mu\text{eV}$ and $\varepsilon = 0$. Dashed lines are fits to cavity input-output theory. Bottom right panel: Cavity reflectance spectrum $|S_{11}|$ of a GaAs-based device taken with $2t_c/h < f_c$. Data in the top panels and bottom left panel of panel **b** are adapted with permission from REF.³⁴, AAAS. Data in the bottom right panel of panel **b** are adapted with permission from REF.³⁵, American Physical Society.

The hallmark of the strong-coupling regime is the vacuum Rabi splitting, which is the emergence of a pair of distinct resonance peaks in the cavity transmission spectrum for a fixed detuning ε where the qubit and a cavity photon become equal in frequency^{6, 7, 10, 41}. The top left panel of FIG. 4b shows a measurement of A/A_0 as a function of f and ε , taken with a Si-based DQD tuned to $2t_c/h = f_c$ (REF³⁴). At a large value of $\varepsilon = 6 \mu\text{eV}$, the cavity transmission spectrum (bottom left panel of FIG. 4b) exhibits a single peak. Here the qubit-photon frequency detuning is large (white dashed lines) and the full-width-at-half-maximum (FWHM) of A^2/A_0^2 gives the bare cavity loss rate $\kappa/2\pi = 1.0 \text{ MHz}$. At $\varepsilon = 0$, the DQD splitting $\Omega = 2t_c = hf_c$ and the charge qubit become entangled with a single photon, leading to an “avoided crossing” in the eigenenergies of the charge-photon system (white solid lines). Correspondingly, vacuum Rabi splitting is observed in the cavity transmission spectrum (bottom left panel of FIG. 4b) where the two resonance modes are separated by a vacuum Rabi frequency $2g_c/2\pi = 13.4 \text{ MHz}$. The top right panel of FIG. 4b shows similar data taken with $2t_c/h < f_c$, in which a pair of avoided crossings are observed when $\Omega/h = f_c$ at finite ε . The clear resolution of the vacuum Rabi splitting suggests that the regime of strong charge-photon coupling has been achieved for this Si-based device – a conclusion further supported by a charge decoherence rate $\gamma_c/2\pi = 2.6 \text{ MHz}$ independently determined using microwave spectroscopy in the dispersive regime^{34, 101}. The charge decoherence rate of this device, about two to three orders of magnitude lower than typical DQD charge qubits^{47, 49, 63, 67, 77-80, 82, 85}, is a subject of ongoing investigation. A more recent work suggests that it may arise from both a low level of charge noise and the effect of valley-orbit hybridization¹⁰².

Strong charge-photon coupling has also been demonstrated with GaAs-based devices, using a SQUID array cavity³⁵. Due to the higher impedance of the microwave cavity, a large charge-photon coupling rate $g_c/2\pi = 119 \text{ MHz}$ is found (bottom right panel of FIG. 4b), which allows the strong-coupling regime to be accessed despite comparatively large values of $\gamma_c/2\pi = 40 \text{ MHz}$ and $\kappa/2\pi = 12 \text{ MHz}$. More recently, a low charge decoherence rate of $\gamma_c/2\pi = 3 \text{ MHz}$ has been achieved by a GaA-based DQD as well⁸⁸.

3. Spin-photon coupling

The quantum coherence of the spin $1/2$ of individual electrons in quantum dots or defects in silicon typically lasts between tens of microseconds to several milliseconds¹⁰³⁻¹⁰⁶ and can in some cases even approach a second¹⁰⁷, while the nuclear spin coherence can last as long as a minute¹⁰⁷. In comparison, the coherence of the charge qubit in a DQD is quite short-lived with a decay time of typically a few nanoseconds⁴⁷⁻⁴⁹. The spin is therefore the primary choice as a qubit for quantum information processing in semiconductors^{108, 109}. Since the exchange interaction is short ranged⁵¹, this naturally leads to the question of how to couple two electron spins that are separated by a large distance using spin-electric coupling to a common cavity mode. At the face of it, this seems very hard because the spin of an electron does not directly couple to the electric field of the cavity. However, there are several techniques to hybridize the spin and charge degrees of freedom (qubits) of an electron. All of these methods endow the spin

with an effective electric dipole that enables its interaction with the electric field of the cavity. For multi-electron spin qubits, the Fermi statistics provides a way to couple orbital and spin degrees of freedom^{12, 110, 111} (a recent experiment using this method has attained strong spin qubit-photon coupling³⁸). One mechanism that works for single electron spins is the natural built-in spin-orbit coupling due to relativistic effects which can be sizeable in a number of semiconductor materials^{13, 112, 113}. The intrinsic spin-orbit coupling may work particularly well for holes in the valence band of some semiconductors¹¹⁴. Without relying on such intrinsic effects, one can engineer a spin-electric interaction using controlled magnetic fields, either time-dependent fields that induce electron spin resonance^{11, 115-117} or static but spatially varying fields produced by an on-chip microscale ferromagnet^{36, 64, 105, 118, 119}. In the case of a static magnetic field gradient $\nabla_x \mathbf{B}$ produced by a micromagnet, an applied electric field E_{ac} will shift the electron position in a single quantum dot by $x_E = eE_{ac}a_0^2/E_{orb}$ where E_{orb} and a_0 denote the energy level spacing and size of the quantum dot. For an oscillatory electric field this means that the magnetic field seen by the electron also becomes oscillatory, $\mathbf{B}(x_0 + x_E \sin \omega t) \sim \mathbf{B}(x_0) + \nabla_x \mathbf{B} x_E \sin \omega t$, allowing for electric dipole spin resonance (EDSR). For the quantized cavity field, one finds that $E_{ac} \sin \omega t$ is replaced by $E_{cav} = E_0(a + a^\dagger)$ resulting in a spin-photon coupling $g_s \sim eE_0 \nabla_x \mathbf{B} a_0^2/E_{orb}$. The spin-phonon coupling g_s in a DQD can be much larger and more controllable than for a single QD. For a symmetric DQD at $\varepsilon = 0$ one finds $g_s \sim eE_0 \nabla_x \mathbf{B} d^2/\Omega \sim g_c \Delta B_x/\Omega$, where d is the distance between the two dots, $\Delta B_x = \nabla_x \mathbf{B} d$ is the change in magnetic field (measured in energy units) from one dot to the other, and the DQD energy splitting Ω can be tuned by the inter-dot tunnel coupling and the external magnetic field⁶⁴. Since $d > a_0$ and $\Omega \ll E_{orb}$, g_s is much larger in a DQD compared to a single dot^{120, 121}.

To study the combined charge and spin dynamics of the spin and charge of a single electron in a DQD one can employ the 4x4 Hamiltonian in the basis $|\uparrow, 0\rangle, |\downarrow, 0\rangle, |0, \uparrow\rangle, |0, \downarrow\rangle$

$$H_0 = \frac{1}{2} \begin{pmatrix} \varepsilon + B_z & \Delta B_x & 2t_c & 0 \\ \Delta B_x & \varepsilon - B_z & 0 & 2t_c \\ 2t_c & 0 & -\varepsilon + B_z & -\Delta B_x \\ 0 & 2t_c & -\Delta B_x & -\varepsilon - B_z \end{pmatrix},$$

which includes the Zeeman coupling $H_z = \mathbf{S} \cdot \mathbf{B}(\mathbf{r})$ of the spin \mathbf{S} to an external magnetic field $\mathbf{B}(\mathbf{r})$ (in energy units) [REF⁶⁴]. A magnetic field B_z pointing in z direction leads to an energy splitting between the spin-up and spin-down states. As long as the field has the same strength in both dots, i.e. \mathbf{B} does not depend on the position \mathbf{r} , the spin and charge qubits are completely separate. In this case, only the charge qubit interacts with the electromagnetic field (photons) of the cavity, while the spin is decoupled from it. However, as soon as a magnetic field difference ΔB_x perpendicular to the homogeneous field component is applied, the charge and spin qubits are hybridized, allowing for a coupling of the spin qubit to the cavity photons. The coupling to the cavity is again obtained by replacing ε with $\varepsilon + eE_{cav}d$ with the cavity electric field $E_{cav} = E_0(a + a^\dagger)$. In this way, we obtain the Hamiltonian $H = H_0 + H_{int}$ with $H_{int} = g_c(a + a^\dagger)\tau_z$ where $g_c = eE_0d$. The four relevant energy levels $|n\rangle$ of the DQD are found by diagonalizing the matrix H_0 , while the electric dipole transition matrix elements d_{nm} can be determined by transforming H_{int} into the eigenbasis of H_0 ,

$$H_{\text{int}} = g_c (a + a^\dagger) \sum_{n,m=0}^3 d_{nm} |n\rangle\langle m|.$$

For the understanding of the most important mechanisms for the spin-photon interaction, it is sufficient to consider an effective two-level model. Making also the rotating wave approximation, one arrives at the Jaynes-Cummings model $H = \frac{1}{2} \Delta_s \sigma_z + g_s (a \sigma_+ + a^\dagger \sigma_-)$, where the σ_z Pauli operators act on the low-energy hybridized spin states, and $\Delta_s = B_z - hf_c$ is the detuning of the spin splitting B_z from the photon energy hf_c . For a symmetric DQD with $\varepsilon = 0$ one finds a spin-photon coupling rate $g_s \cong g_c \Delta B_x / (2 \delta)$ where $\delta = 2t_c - hf_c$ can be controlled by adjusting the tunnel coupling t_c between the two quantum dots. While this two-level model explains the vacuum Rabi splitting that has been observed experimentally, there are more subtle effects such as the asymmetry of the Rabi peak heights that require a three-level model for their explanation⁶⁴.

Strong spin-photon coupling

Compared to charge-photon coupling, reaching the strong-coupling regime of spin-photon interaction faces a distinct challenge: The direct magnetic-dipole coupling rate g_s between a single electron spin and a single photon is mostly limited to between 10 Hz and 500 Hz, which is too slow to overcome single-spin dephasing rates or cavity loss rates^{44, 45, 122-125}. As such, a robust scheme for spin-charge hybridization is necessary to increase g_s to the MHz range where strong-coupling becomes feasible^{11-13, 64, 110, 111, 120, 121, 126-128}. At the same time, a low level of charge noise is required of the device since spin-charge hybridization subjects the electron spin to charge-noise-induced dephasing. A cavity-coupled carbon nanotube DQD in an earlier experiment hybridized spin and charge via ferromagnetic leads to achieve $g_s/2\pi = 1.3$ MHz, but was still in the weak-coupling regime due to a larger spin decoherence rate $\gamma_s/2\pi = 2.5$ MHz (REF¹²⁹). More recently, two experiments using Si-based DQDs have successfully attained the strong-coupling regime between a single spin and a single photon^{36, 37}. We review these results in this section.

The setup for one of the experiments³⁶ is illustrated in FIG. 5a. The device is a gate-defined DQD on top of a Si/SiGe heterostructure coupled to a co-planar waveguide cavity, similar to the previous work on strong charge-photon coupling³⁴ but including a crucial new ingredient: the addition of a micron-sized Co magnet on top^{103, 130, 131}. When magnetized by an externally applied magnetic field B_z^{ext} , the fringing field of the micromagnet creates a large gradient for the magnetic field component pointing along the x -axis, i.e., a large $\partial B_x / \partial z$. As such, the quantization axis of the electron spin is dependent on its location, hybridizing the spin and charge degrees of freedom^{13, 64, 120, 121, 128}. A plot of the DQD energy levels including the spin degree of freedom is provided in FIG. 5b, which is helpful for discussing the experimental results below.

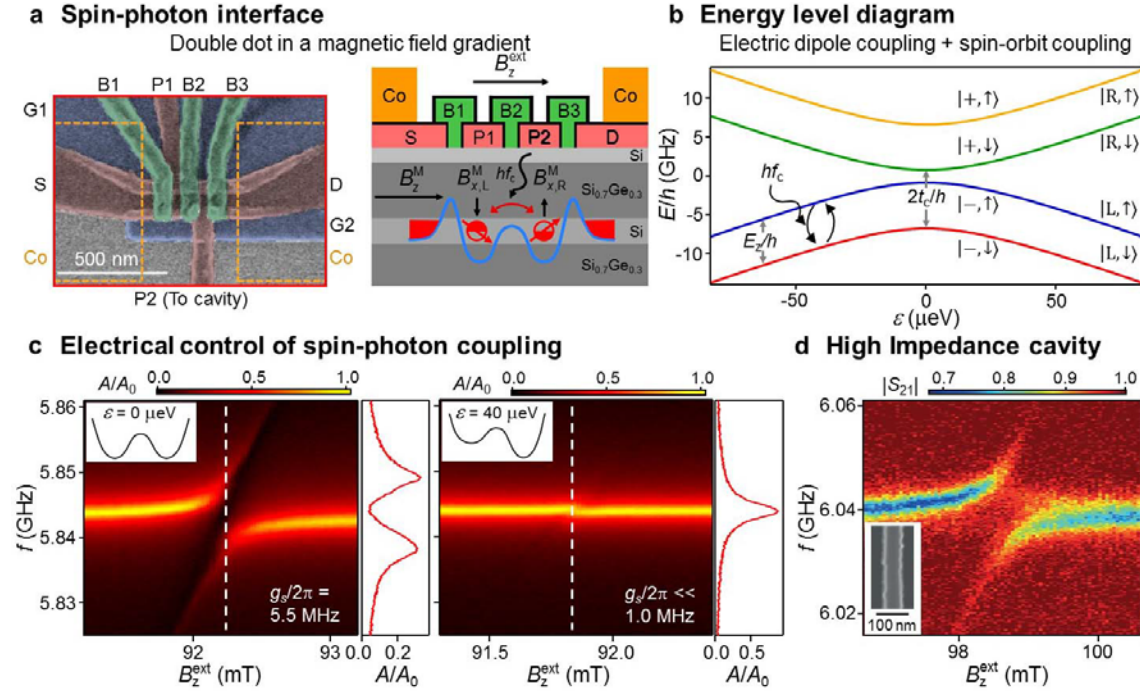


Figure 5 | **Strong spin-photon coupling.** **a** | Top left panel: SEM image of a Si/SiGe DQD used to achieve spin-photon coupling. The orange dashed lines represent the locations of a pair of Co micromagnets fabricated on top of the DQD. Top right panel shows a cross-sectional view of the device. The application of an external magnetic field B_z^{ext} polarizes the micromagnets and creates an inhomogeneous magnetic field having a component B_z^{M} parallel to B_z^{ext} and a component B_x^{M} orthogonal to B_z^{ext} . B_x^{M} changes sign between the two dots, assuming a value of $B_{x,L}^{\text{M}}$ for the left dot and $B_{x,R}^{\text{M}}$ for the right dot. As a result, the quantization axis of an electron's spin (red arrows) is dependent on the electron's position. **b** | Energy level diagram of a single electron trapped in a DQD in the presence of an inhomogeneous magnetic field as a function of the DQD detuning energy ε . Here \uparrow and \downarrow denote the Zeeman-split spin-states of the electron, L (R) denotes the single-dot orbital state of the left (right) dot and $-$ ($+$) denotes the molecular bonding (anti-bonding) state formed by the hybridization of the L and R states. **c** | Left panel: Cavity transmission amplitude A/A_0 as a function of f and B_z^{ext} . Vacuum Rabi splitting with a frequency $2g_s/2\pi = 11.0$ MHz is observed at $B_z^{\text{ext}} = 92.2$ mT. Right panel: Increasing the detuning to $\varepsilon = 40$ μeV greatly reduces the vacuum Rabi splitting, allowing for electrical control of the spin-photon coupling rate. **d** | Strong spin-photon coupling using a high impedance NbTiN nanowire resonator. The cavity transmission coefficient $|S_{21}|$ is plotted as a function of f and B_z^{ext} . Inset: Scanning electron microscope image of a portion of the NbTiN nanowire resonator. Panels **a**, **b** and **c** are adapted from REF.³⁶, Macmillan Publishers Limited. Panel **d** is adapted with permission from REF.³⁷, AAAS.

To search for spin-photon coupling, the frequency of the single-spin qubit $E_Z/h = g\mu_B B_{\text{tot}}/h$ is tuned into resonance with the cavity by changing the external magnetic field B_z^{ext} . Here E_Z is the Zeeman energy, g is the g -factor of the electron and μ_B is the Bohr magneton. B_{tot} is the total magnetic field spatially averaged over the electron's wavefunction, having contributions from both the externally applied field and the intrinsic field of the micromagnet. The left panel of FIG. 5c shows the cavity transmission amplitude A/A_0 as a function of f and B_z^{ext} , taken at $\varepsilon = 0$. A clear avoided crossing is observed around $B_z^{\text{ext}} = 92.2$ mT, where the resonance condition $E_Z/h = f_c$ is met. A plot of A/A_0 as a function of f at $B_z^{\text{ext}} = 92.2$ mT again shows vacuum Rabi splitting with a frequency $2g_s/2\pi = 11.0$ MHz (left panel of FIG. 5c), signifying strong-coupling between the single electron spin and a cavity photon. The spin-photon coupling rate $g_s/2\pi = 5.5$ MHz observed here exceeds direct magnetic-dipole coupling rates by four to five orders of magnitude^{44, 45, 122-125}. This remarkable enhancement in g_s may be understood by considering the energy diagram in FIG. 5b. In the regime $|\varepsilon| \ll t_c$, the single-dot orbital states L and R are hybridized by the interdot tunnel coupling t_c to form molecular bonding and anti-bonding states (see discussion in Box 1). While occupying these charge states, the electron wavefunction becomes delocalized across the two dots and the electric field of a cavity photon can displace its wavefunction by about 1 nm, generating a large effective magnetic field due to the magnetic field gradient and yielding a large g_s (REF³⁶).

A second experiment, also involving a DQD defined on a Si/SiGe heterostructure, uses a cavity design composed of a thin NbTiN nanowire with a large kinetic inductance (inset to FIG. 5d)³⁷. A higher impedance in the kilo-ohm range is supported by this cavity. Strong spin-photon coupling is also achieved by this device, as shown by the avoided crossing in FIG. 5d.

To apply the spin-photon cavity QED device to quantum information processing, it is also necessary to rapidly switch on and off the spin-photon coupling rate g_s . This flexibility would allow the spin qubit to be manipulated in an isolated state ($g_s \approx 0$) where it is protected from cavity-induced Purcell decay^{123, 132-134} and read out via the cavity when the coupling is back on. One way to tune g_s is by tilting the DQD potential, as shown in FIG. 5c. As ε is increased from zero, we observe a strong decrease of spin-photon coupling from $g_s/2\pi = 5.5$ MHz ($\varepsilon = 0$) to $g_s/2\pi \ll 1$ MHz ($\varepsilon = 40$ μeV). This change is due to the fact that at $|\varepsilon| \gg t_c$, the electron wavefunction becomes strongly localized within one dot (FIG. 5b) and interdot tunneling is largely suppressed. Here the displacement of the electron wavefunction by the cavity photon is limited to about 3 pm in distance³⁶. The effective magnetic field generated by a cavity photon is therefore very small, effectively turning off spin-photon coupling. Using nanosecond control of ε , driven Rabi oscillation and dispersive readout of the single-spin qubit have been demonstrated³⁶, paving the way toward quantum non-demolition readout of spin qubits¹³⁵ which may allow error-correction codes such as the surface code to be implemented with spin qubits^{136, 137}.

4. Outlook/Conclusions

Where do these exciting developments lead us? The strong and controllable coupling between individual spin qubits embedded in a superconducting microwave resonator allows for long-distance spin-spin coupling mediated by microwave photons^{138, 139}. This coupling can then be employed to perform entangling two-qubit gates between spins separated by several millimeters. One should keep in mind that one millimeter is a very long distance compared with the 80 nm separation of nearest-neighbor spin qubits in Si¹⁴⁰. Their small footprint on a semiconductor chip is one characteristic feature of semiconductor spin qubits which makes them strong contenders for a scalable quantum information processing platform. In addition to providing the possibility to entangle distant spin qubits, non-local two-qubit gates may facilitate quantum error correction in the framework of a fault-tolerant quantum computing architecture. Also in this context, the possibility of creating a network of spin qubits with engineered coupling may be very useful for realizing a surface code¹³⁶. Moreover, the possibility of creating a network of spin qubits with coupling geometries ranging from local to “all-to-all” opens interesting perspectives for quantum simulation of interacting quantum many-body systems^{141, 142}.

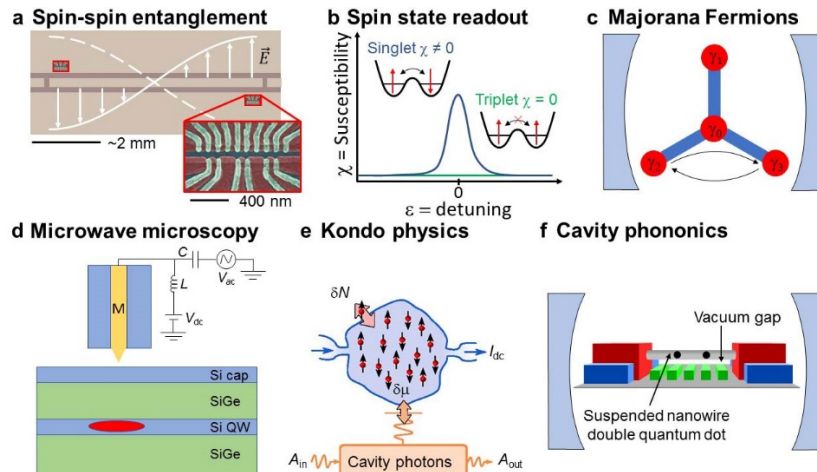


Figure 6 | **Future directions in “super-semi” circuit QED.** **a** | A future spin-based quantum processor could consist of local nodes of nearest-neighbor exchange coupled spins. Long distance coupling of the nodes could be achieved using spin-photon coupling. **b** | The charge susceptibility of a two-electron DQD is dependent on the electron spin configuration, leading quite naturally to cavity-based readout of electron spin states. **c** | Circuit QED has been proposed as a platform to allow for braiding of Majorana Fermions. **d** | Scanning microwave impedance microscope based on circuit QED. In this example the evanescent field from a scannable superconducting resonator is used to probe the valley splitting in a quantum dot that is induced beneath the scanning probe. **e** | Circuit QED may be used to probe Kondo physics in carbon nanotubes. The measurement technique may also shed light on other exotic states of matter. **f** | The transmission through a superconducting cavity has been shown to be sensitive to mechanical degrees of freedom. Coherent conversion from optical to microwave frequencies has been attempted using circuit QED devices incorporating mechanical resonators.

Spin-photon coupling has important implications beyond the generation of long-range quantum entanglement (FIG. 6a). The coupling of the electron spin to an electromagnetic cavity also allows for the dispersive readout of the quantum state of the spin qubit^{36, 67} and lays the groundwork for the development of quantum non-demolition^{135, 143} and single-shot readout methods¹⁴⁴. Since the spin-photon coupling gate g_s is a strong function of detuning ε , electrically switching on the cavity coupling of each spin qubit³⁴ may allow for selective readout in large arrays of spin qubits (FIG. 6b). Moreover, the superconducting qubit community has adopted the use of frequency multiplexed resonators^{21, 145} for quantum state readout. A similar approach could be adopted for spins¹⁴⁶.

Looking well beyond spin qubits, the nascent field of hybrid circuit quantum electrodynamics could have a major impact on condensed matter physics as a whole. Some potential areas of research are illustrated in FIG. 6. Cavity measurements have been proposed to investigate Majorana modes¹⁴⁷ and provide an alternative to the somewhat ambiguous measurements of zero-bias conductance peaks¹⁴⁸⁻¹⁵¹. It has even been suggested that microwave cavities could be used to implement braiding of Majorana Fermions¹⁵² (FIG. 6c). Scanning-probe versions of superconducting cavities (FIG. 6d) could be used to probe valley physics in silicon¹⁵³⁻¹⁵⁶ and perhaps be of much broader use in investigations of two-dimensional quantum materials¹⁵⁷. Lastly, superconducting cavities have been shown to provide an alternative means to investigate Kondo physics¹⁵⁸⁻¹⁶⁰ (FIG. 6e) and electron-phonon coupling^{161, 162} (FIG. 6f). Clearly these applications are just scratching the surface and there are many unopened areas of investigation, including, for example, spin-charge separation in Luttinger liquids¹⁶³⁻¹⁶⁵ and THz probes of topological phases of matter¹⁶⁶.

References

1. Haroche, S. & Kleppner, D. Cavity Quantum Electrodynamics. *Phys. Today* **42**, 24 (1989).
2. Miller, R. et al. Trapped atoms in cavity QED: coupling quantized light and matter. *J. Phys. B* **38**, S551 (2005).
3. Walther, H., Varcoe, B.T.H., Englert, B.-G. & Becker, T. Cavity quantum electrodynamics. *Rep. Prog. Phys.* **69**, 1325 (2006).
4. Haroche, S. & Raimond, J.M. Exploring the quantum: atoms, cavities and photons (Oxford University Press, New York, 2006).
5. Brune, M. et al. Observing the Progressive Decoherence of the "Meter" in a Quantum Measurement. *Phys. Rev. Lett.* **77**, 4887 (1996).
6. Reithmaier, J.P. et al. Strong coupling in a single quantum dot–semiconductor microcavity system. *Nature* **432**, 197 (2004).
7. Yoshie, T. et al. Vacuum Rabi splitting with a single quantum dot in a photonic crystal nanocavity. *Nature* **432**, 200 (2004).
8. Peter, E. et al. Exciton-photon strong-coupling regime for a single quantum dot embedded in a microcavity. *Phys. Rev. Lett.* **95**, 067401 (2005).
9. Blais, A., Huang, R.-S., Wallraff, A., Girvin, S.M. & Schoelkopf, R.J. Cavity quantum electrodynamics for superconducting electrical circuits: An architecture for quantum computation. *Phys. Rev. A* **69**, 062320 (2004).
10. Wallraff, A. et al. Strong coupling of a single photon to a superconducting qubit using circuit quantum electrodynamics. *Nature* **431**, 162 (2004).
11. Childress, L., Sørensen, A.S. & Lukin, M.D. Mesoscopic cavity quantum electrodynamics with quantum dots. *Phys. Rev. A* **69**, 042302 (2004).
12. Burkard, G. & Imamoglu, A. Ultra-long-distance interaction between spin qubits. *Phys. Rev. B* **74**, 041307 (2006).
13. Trif, M., Golovach, V.N. & Loss, D. Spin dynamics in InAs nanowire quantum dots coupled to a transmission line. *Phys. Rev. B* **77**, 045434 (2008).
14. Majer, J. et al. Coupling superconducting qubits via a cavity bus. *Nature* **449**, 443 (2007).
15. Sillanpaa, M.A., Park, J.I. & Simmonds, R.W. Coherent quantum state storage and transfer between two phase qubits via a resonant cavity. *Nature* **449**, 438 (2007).
16. Neeley, M. et al. Generation of three-qubit entangled states using superconducting phase qubits. *Nature* **467**, 570 (2010).
17. Reed, M.D. et al. Realization of three-qubit quantum error correction with superconducting circuits. *Nature* **482**, 382 (2012).
18. Fedorov, A., Steffen, L., Baur, M., da Silva, M.P. & Wallraff, A. Implementation of a Toffoli gate with superconducting circuits. *Nature* **481**, 170 (2012).
19. Saira, O.P. et al. Entanglement Genesis by Ancilla-Based Parity Measurement in 2D Circuit QED. *Phys. Rev. Lett.* **112**, 070502 (2014).
20. Wallraff, A. et al. Approaching Unit Visibility for Control of a Superconducting Qubit with Dispersive Readout. *Phys. Rev. Lett.* **95**, 060501 (2005).
21. Heinsoo, J. et al. Rapid High-fidelity Multiplexed Readout of Superconducting Qubits. *Phys. Rev. Applied* **10**, 034040 (2018).
22. Reed, M.D. et al. High-Fidelity Readout in Circuit Quantum Electrodynamics Using the Jaynes-Cummings Nonlinearity. *Phys. Rev. Lett.* **105**, 173601 (2010).

23. Eichler, C. et al. Experimental state tomography of itinerant single microwave photons. *Phys. Rev. Lett.* **106**, 220503 (2011).
24. Houck, A.A. et al. Generating single microwave photons in a circuit. *Nature* **449**, 328 (2007).
25. Hofheinz, M. et al. Generation of Fock states in a superconducting quantum circuit. *Nature* **454**, 310 (2008).
26. Vlastakis, B. et al. Deterministically encoding quantum information using 100-photon Schrodinger cat states. *Science* **342**, 607 (2013).
27. Wang, C. et al. A Schrodinger cat living in two boxes. *Science* **352**, 1087 (2016).
28. Riste, D., Bultink, C.C., Lehnert, K.W. & DiCarlo, L. Feedback control of a solid-state qubit using high-fidelity projective measurement. *Phys. Rev. Lett.* **109**, 240502 (2012).
29. Campagne-Ibarcq, P. et al. Persistent Control of a Superconducting Qubit by Stroboscopic Measurement Feedback. *Phys. Rev. X* **3**, 021008 (2013).
30. Murch, K.W., Weber, S.J., Macklin, C. & Siddiqi, I. Observing single quantum trajectories of a superconducting quantum bit. *Nature* **502**, 211 (2013).
31. Tyryshkin, A.M. et al. Electron spin coherence exceeding seconds in high-purity silicon. *Nat. Mater.* **11**, 143 (2011).
32. Maurer, P.C. et al. Room-temperature quantum bit memory exceeding one second. *Science* **336**, 1283 (2012).
33. Saeedi, K. et al. Room-temperature quantum bit storage exceeding 39 minutes using ionized donors in silicon-28. *Science* **342**, 830 (2013).
34. Mi, X., Cady, J.V., Zajac, D.M., Deelman, P.W. & Petta, J.R. Strong coupling of a single electron in silicon to a microwave photon. *Science* **355**, 156 (2017).
35. Stockklauser, A. et al. Strong Coupling Cavity QED with Gate-Defined Double Quantum Dots Enabled by a High Impedance Resonator. *Phys. Rev. X* **7**, 011030 (2017).
36. Mi, X. et al. A coherent spin–photon interface in silicon. *Nature* **555**, 599 (2018).
37. Samkharadze, N. et al. Strong spin-photon coupling in silicon. *Science* **359**, 1123 (2018).
38. Landig, A.J. et al. Coherent spin–photon coupling using a resonant exchange qubit. *Nature* **560**, 179 (2018).
39. Hulet, R.G., Hilfer, E.S. & Kleppner, D. Inhibited spontaneous emission by a Rydberg atom. *Phys. Rev. Lett.* **55**, 2137 (1985).
40. Jhe, W. et al. Suppression of spontaneous decay at optical frequencies: Test of vacuum-field anisotropy in confined space. *Phys. Rev. Lett.* **58**, 666 (1987).
41. Thompson, R.J., Rempe, G. & Kimble, H.J. Observation of normal-mode splitting for an atom in an optical cavity. *Phys. Rev. Lett.* **68**, 1132 (1992).
42. Englund, D. et al. Deterministic coupling of a single nitrogen vacancy center to a photonic crystal cavity. *Nano Lett.* **10**, 3922 (2010).
43. Kubo, Y. et al. Strong coupling of a spin ensemble to a superconducting resonator. *Phys. Rev. Lett.* **105**, 140502 (2010).
44. Schuster, D.I. et al. High-Cooperativity Coupling of Electron-Spin Ensembles to Superconducting Cavities. *Phys. Rev. Lett.* **105**, 140501 (2010).
45. Amsüss, R. et al. Cavity QED with Magnetically Coupled Collective Spin States. *Phys. Rev. Lett.* **107**, 060502 (2011).
46. Sipahigil, A. et al. An integrated diamond nanophotonics platform for quantum-optical networks. *Science* **354**, 847 (2016).

47. Hayashi, T., Fujisawa, T., Cheong, H.D., Jeong, Y.H. & Hirayama, Y. Coherent Manipulation of Electronic States in a Double Quantum Dot. *Phys. Rev. Lett.* **91**, 226804 (2003).
48. Petta, J.R., Johnson, A.C., Marcus, C.M., Hanson, M.P. & Gossard, A.C. Manipulation of a Single Charge in a Double Quantum Dot. *Phys. Rev. Lett.* **93**, 186802 (2004).
49. Petersson, K.D., Petta, J.R., Lu, H. & Gossard, A.C. Quantum Coherence in a One-Electron Semiconductor Charge Qubit. *Phys. Rev. Lett.* **105**, 246804 (2010).
50. Koppens, F.H.L. et al. Driven coherent oscillations of a single electron spin in a quantum dot. *Nature* **442**, 766 (2006).
51. Petta, J.R. et al. Coherent manipulation of coupled electron spins in semiconductor quantum dots. *Science* **309**, 2180 (2005).
52. Clarke, J. & Wilhelm, F.K. Superconducting quantum bits. *Nature* **453**, 1031 (2008).
53. Nakamura, Y., Pashkin, Y.A. & Tsai, J.S. Coherent control of macroscopic quantum states in a single-Cooper-pair box. *Nature* **398**, 786 (1999).
54. Vion, D. et al. Manipulating the quantum state of an electrical circuit. *Science* **296**, 886 (2002).
55. Koch, J. et al. Charge-insensitive qubit design derived from the Cooper pair box. *Phys. Rev. A* **76**, 042319 (2007).
56. Krantz, P. et al. A Quantum Engineer's Guide to Superconducting Qubits *arXiv:1904.06560* (2019).
57. Martinis, J.M., Nam, S., Aumentado, J. & Urbina, C. Rabi oscillations in a large Josephson-junction qubit. *Phys. Rev. Lett.* **89** (2002).
58. Devoret, M.H. & Schoelkopf, R.J. Superconducting circuits for quantum information: an outlook. *Science* **339**, 1169 (2013).
59. Xiang, Z.-L., Ashhab, S., You, J.Q. & Nori, F. Hybrid quantum circuits: Superconducting circuits interacting with other quantum systems. *Rev. Mod. Phys.* **85**, 623 (2013).
60. van der Wiel, W.G. et al. Electron transport through double quantum dots. *Rev. Mod. Phys.* **75**, 1 (2002).
61. Hanson, R., Kouwenhoven, L.P., Petta, J.R., Tarucha, S. & Vandersypen, L.M.K. Spins in few-electron quantum dots. *Rev. Mod. Phys.* **79**, 1217 (2007).
62. Sohn, L.L., Kouwenhoven, L.P. & Schön, G. Mesoscopic electron transport (Kluwer Academic Publishers, Boston, 1997).
63. Kim, D. et al. Microwave-driven coherent operation of a semiconductor quantum dot charge qubit. *Nat. Nanotechnol.* **10**, 243 (2015).
64. Benito, M., Mi, X., Taylor, J.M., Petta, J.R. & Burkard, G. Input-output theory for spin-photon coupling in Si double quantum dots. *Phys. Rev. B* **96**, 235434 (2017).
65. Clerk, A.A., Devoret, M.H., Girvin, S.M., Marquardt, F. & Schoelkopf, R.J. Introduction to quantum noise, measurement, and amplification. *Rev. Mod. Phys.* **82**, 1155 (2010).
66. Walls, D. & Milburn, G. Quantum Optics (Springer, Berlin, 2008).
67. Petersson, K.D. et al. Circuit quantum electrodynamics with a spin qubit. *Nature* **490**, 380 (2012).
68. Petersson, K.D. et al. Charge and Spin State Readout of a Double Quantum Dot Coupled to a Resonator. *Nano Lett.* **10**, 2789 (2010).
69. Chorley, S.J. et al. Measuring the Complex Admittance of a Carbon Nanotube Double Quantum Dot. *Phys. Rev. Lett.* **108**, 036802 (2012).

70. Schroer, M.D., Jung, M., Petersson, K.D. & Petta, J.R. Radio Frequency Charge Parity Meter. *Phys. Rev. Lett.* **109**, 166804 (2012).
71. Jung, M., Schroer, M.D., Petersson, K.D. & Petta, J.R. Radio frequency charge sensing in InAs nanowire double quantum dots. *Appl. Phys. Lett.* **100**, 253508 (2012).
72. Frey, T. et al. Quantum dot admittance probed at microwave frequencies with an on-chip resonator. *Phys. Rev. B* **86**, 115303 (2012).
73. Meystre, P. & Sargent, M. Elements of quantum optics (Springer, Berlin, 2007).
74. Raimond, J.M., Brune, M. & Haroche, S. Manipulating quantum entanglement with atoms and photons in a cavity. *Rev. Mod. Phys.* **73**, 565 (2001).
75. Eberly, J.H., Narozhny, N.B. & Sanchez-Mondragon, J.J. Periodic Spontaneous Collapse and Revival in a Simple Quantum Model. *Phys. Rev. Lett.* **44**, 1323 (1980).
76. Cirac, J.I. & Zoller, P. Quantum Computations with Cold Trapped Ions. *Phys. Rev. Lett.* **74**, 4091 (1995).
77. Frey, T. et al. Dipole Coupling of a Double Quantum Dot to a Microwave Resonator. *Phys. Rev. Lett.* **108**, 046807 (2012).
78. Toida, H., Nakajima, T. & Komiyama, S. Vacuum Rabi Splitting in a Semiconductor Circuit QED System. *Phys. Rev. Lett.* **110**, 066802 (2013).
79. Stockklauser, A. et al. Microwave Emission from Hybridized States in a Semiconductor Charge Qubit. *Phys. Rev. Lett.* **115**, 046802 (2015).
80. Basset, J. et al. Single-electron double quantum dot dipole-coupled to a single photonic mode. *Phys. Rev. B* **88**, 125312 (2013).
81. Liu, Y.-Y. et al. Semiconductor double quantum dot micromaser. *Science* **347**, 285 (2015).
82. Deng, G.-W. et al. Charge Number Dependence of the Dephasing Rates of a Graphene Double Quantum Dot in a Circuit QED Architecture. *Phys. Rev. Lett.* **115**, 126804 (2015).
83. Deng, G.-W. et al. Coupling Two Distant Double Quantum Dots with a Microwave Resonator. *Nano Lett.* **15**, 6620-6625 (2015).
84. Delbecq, M.R. et al. Coupling a Quantum Dot, Fermionic Leads, and a Microwave Cavity on a Chip. *Phys. Rev. Lett.* **107**, 256804 (2011).
85. Viennot, J.J., Delbecq, M.R., Dartailh, M.C., Cottet, A. & Kontos, T. Out-of-equilibrium charge dynamics in a hybrid circuit quantum electrodynamics architecture. *Phys. Rev. B* **89**, 165404 (2014).
86. Mi, X. et al. Circuit quantum electrodynamics architecture for gate-defined quantum dots in silicon. *Appl. Phys. Lett.* **110**, 043502 (2017).
87. Schuster, D.I. et al. Resolving photon number states in a superconducting circuit. *Nature* **445**, 515 (2007).
88. Scarlino, P. et al. All-Microwave Control and Dispersive Readout of Gate-Defined Quantum Dot Qubits in Circuit Quantum Electrodynamics. *arXiv:1711.01906* (2017).
89. Stehlik, J. et al. Double Quantum Dot Floquet Gain Medium. *Phys. Rev. X* **6**, 041027 (2016).
90. Viennot, J.J., Palomo, J. & Kontos, T. Stamping single wall nanotubes for circuit quantum electrodynamics. *Appl. Phys. Lett.* **104**, 113108 (2014).
91. Milonni, P.W. The quantum vacuum: An introduction to quantum electrodynamics (Academic Press, Boston, 1994).

92. Day, P.K., LeDuc, H.G., Mazin, B.A., Vayonakis, A. & Zmuidzinas, J. A broadband superconducting detector suitable for use in large arrays. *Nature* **425**, 817 (2003).
93. Göppl, M. et al. Coplanar waveguide resonators for circuit quantum electrodynamics. *J. Appl. Phys.* **104**, 113904 (2008).
94. Stehlik, J. et al. Fast Charge Sensing of a Cavity-Coupled Double Quantum Dot Using a Josephson Parametric Amplifier. *Phys. Rev. Applied* **4**, 014018 (2015).
95. Samkharadze, N. et al. High-Kinetic-Inductance Superconducting Nanowire Resonators for Circuit QED in a Magnetic Field. *Phys. Rev. Applied* **5**, 044004 (2016).
96. Wallraff, A., Stockklauser, A., Ihn, T., Petta, J.R. & Blais, A. Comment on "Vacuum Rabi Splitting in a Semiconductor Circuit QED System". *Phys. Rev. Lett.* **111**, 249701 (2013).
97. Basset, J. et al. Evaluating charge noise acting on semiconductor quantum dots in the circuit quantum electrodynamics architecture. *Appl. Phys. Lett.* **105**, 063105 (2014).
98. Field, M. et al. Measurements of Coulomb blockade with a noninvasive voltage probe. *Phys. Rev. Lett.* **70**, 1311 (1993).
99. Sprinzak, D., Ji, Y., Heiblum, M., Mahalu, D. & Shtrikman, H. Charge Distribution in a Kondo-Correlated Quantum Dot. *Phys. Rev. Lett.* **88**, 176805 (2002).
100. Elzerman, J.M. et al. Few-electron quantum dot circuit with integrated charge read out. *Phys. Rev. B* **67**, 161308 (2003).
101. Schuster, D.I. et al. ac Stark Shift and Dephasing of a Superconducting Qubit Strongly Coupled to a Cavity Field. *Phys. Rev. Lett.* **94**, 123602 (2005).
102. Mi, X., Kohler, S. & Petta, J.R. Landau-Zener interferometry of valley-orbit states in Si/SiGe double quantum dots. *Phys. Rev. B* **98**, 161404(R) (2018).
103. Kawakami, E. et al. Electrical control of a long-lived spin qubit in a Si/SiGe quantum dot. *Nat. Nanotechnol.* **9**, 666 (2014).
104. Veldhorst, M. et al. An addressable quantum dot qubit with fault-tolerant control-fidelity. *Nat. Nanotechnol.* **9**, 981 (2014).
105. Yoneda, J. et al. A quantum-dot spin qubit with coherence limited by charge noise and fidelity higher than 99.9%. *Nat. Nanotechnol.* **13**, 102 (2018).
106. Zajac, D.M. et al. Resonantly driven CNOT gate for electron spins. *Science* **359**, 439 (2018).
107. Muhonen, J.T. et al. Storing quantum information for 30 seconds in a nanoelectronic device. *Nat. Nanotechnol.* **9**, 986 (2014).
108. Kane, B.E. A silicon-based nuclear spin quantum computer. *Nature* **393**, 133 (1998).
109. Loss, D. & DiVincenzo, D.P. Quantum computation with quantum dots. *Phys. Rev. A* **57**, 120 (1998).
110. Taylor, J.M., Srinivasa, V. & Medford, J. Electrically Protected Resonant Exchange Qubits in Triple Quantum Dots. *Phys. Rev. Lett.* **111**, 050502 (2013).
111. Russ, M. & Burkard, G. Long distance coupling of resonant exchange qubits. *Phys. Rev. B* **92**, 205412 (2015).
112. Golovach, V.N., Borhani, M. & Loss, D. Electric-dipole-induced spin resonance in quantum dots. *Phys. Rev. B* **74**, 165319 (2006).
113. Rashba, E.I. & Efros, A.L. Orbital mechanisms of electron-spin manipulation by an electric field. *Phys. Rev. Lett.* **91**, 126405 (2003).
114. Kloeffel, C., Trif, M., Stano, P. & Loss, D. Circuit QED with hole-spin qubits in Ge/Si nanowire quantum dots. *Phys. Rev. B* **88**, 241405 (2013).

115. Nowack, K.C., Koppens, F.H.L., Nazarov, Y.V. & Vandersypen, L.M.K. Coherent control of a single electron spin with electric fields. *Science* **318**, 1430 (2007).
116. Nadj-Perge, S., Frolov, S.M., Bakkers, E. & Kouwenhoven, L.P. Spin-orbit qubit in a semiconductor nanowire. *Nature* **468**, 1084 (2010).
117. Schroer, M.D., Petersson, K.D., Jung, M. & Petta, J.R. Field Tuning the g Factor in InAs Nanowire Double Quantum Dots. *Phys. Rev. Lett.* **107**, 176811 (2011).
118. Brunner, R. et al. Two-qubit gate of combined single-spin rotation and interdot spin exchange in a double quantum dot. *Phys. Rev. Lett.* **107**, 146801 (2011).
119. Nakajima, T. et al. Robust Single-Shot Spin Measurement with 99.5% Fidelity in a Quantum Dot Array. *Phys. Rev. Lett.* **119**, 017701 (2017).
120. Cottet, A. & Kontos, T. Spin Quantum Bit with Ferromagnetic Contacts for Circuit QED. *Phys. Rev. Lett.* **105**, 160502 (2010).
121. Hu, X., Liu, Y.-x. & Nori, F. Strong coupling of a spin qubit to a superconducting stripline cavity. *Phys. Rev. B* **86**, 035314 (2012).
122. Imamoğlu, A. Cavity QED Based on Collective Magnetic Dipole Coupling: Spin Ensembles as Hybrid Two-Level Systems. *Phys. Rev. Lett.* **102**, 083602 (2009).
123. Bienfait, A. et al. Controlling spin relaxation with a cavity. *Nature* **531**, 74 (2016).
124. Eichler, C., Sigillito, A.J., Lyon, S.A. & Petta, J.R. Electron Spin Resonance at the Level of 10^4 Spins Using Low Impedance Superconducting Resonators. *Phys. Rev. Lett.* **118**, 037701 (2017).
125. Probst, S. et al. Inductive-detection electron-spin resonance spectroscopy with 65 spins/ $\sqrt{\text{Hz}}$ sensitivity. *Appl. Phys. Lett.* **111**, 202604 (2017).
126. Jin, P.-Q., Marthaler, M., Shnirman, A. & Schön, G. Strong Coupling of Spin Qubits to a Transmission Line Resonator. *Phys. Rev. Lett.* **108**, 190506 (2012).
127. Srinivasa, V., Taylor, J.M. & Tahan, C. Entangling distant resonant exchange qubits via circuit quantum electrodynamics. *Phys. Rev. B* **94**, 205421 (2016).
128. Félix, B., Dany, L.-Q., Coish, W.A. & Michel, P.-L. Coupling a single electron spin to a microwave resonator: controlling transverse and longitudinal couplings. *Nanotechnol.* **27**, 464003 (2016).
129. Viennot, J.J., Dartiailh, M.C., Cottet, A. & Kontos, T. Coherent coupling of a single spin to microwave cavity photons. *Science* **349**, 408 (2015).
130. Pioro-Ladrière, M. et al. Electrically driven single-electron spin resonance in a slanting Zeeman field. *Nat. Phys.* **4**, 776 (2008).
131. Takeda, K. et al. A fault-tolerant addressable spin qubit in a natural silicon quantum dot. *Sci. Adv.* **2**, e1600694 (2016).
132. Purcell, E.M. Spontaneous emission probabilities at radio frequencies. *Phys. Rev.* **69**, 681 (1946).
133. Goy, P., Raimond, J.M., Gross, M. & Haroche, S. Observation of Cavity-Enhanced Single-Atom Spontaneous Emission. *Phys. Rev. Lett.* **50**, 1903 (1983).
134. Heinzen, D.J., Childs, J.J., Thomas, J.E. & Feld, M.S. Enhanced and inhibited visible spontaneous emission by atoms in a confocal resonator. *Phys. Rev. Lett.* **58**, 1320 (1987).
135. Lupaşcu, A. et al. Quantum non-demolition measurement of a superconducting two-level system. *Nat. Phys.* **3**, 119 (2007).
136. Fowler, A.G., Mariantoni, M., Martinis, J.M. & Cleland, A.N. Surface codes: Towards practical large-scale quantum computation. *Phys. Rev. A* **86**, 032324 (2012).

137. Nigg, S.E., Fuhrer, A. & Loss, D. Superconducting Grid-Bus Surface Code Architecture for Hole-Spin Qubits. *Phys. Rev. Lett.* **118**, 147701 (2017).
138. Warren, A., Barnes, E. & Economou, S. Long-distance entangling gates between quantum dot spins mediated by a superconducting resonator. *arXiv:1902.05704* (2019).
139. Benito, M., Petta, J. & Burkard, G. Optimized cavity-mediated dispersive two-qubit gates between spin qubits. *arXiv:1902.07649* (2019).
140. Zajac, D.M., Hazard, T.M., Mi, X., Nielsen, E. & Petta, J.R. Scalable Gate Architecture for a One-Dimensional Array of Semiconductor Spin Qubits. *Phys. Rev. Applied* **6**, 054013 (2016).
141. Georgescu, I.M., Ashhab, S. & Nori, F. Quantum simulation. *Rev. Mod. Phys.* **86**, 153 (2014).
142. Hensgens, T. et al. Quantum simulation of a Fermi-Hubbard model using a semiconductor quantum dot array. *Nature* **548**, 70 (2017).
143. Besse, J.C. et al. Single-Shot Quantum Nondemolition Detection of Individual Itinerant Microwave Photons. *Phys. Rev. X* **8**, 021003 (2018).
144. Zheng, G. et al. Rapid high-fidelity gate-based spin read-out in silicon. *arXiv:1901.00687* (2019).
145. Chen, Y. et al. Multiplexed dispersive readout of superconducting phase qubits. *Appl. Phys. Lett.* **101**, 182601 (2012).
146. Hornibrook, J.M. et al. Frequency multiplexing for readout of spin qubits. *Appl. Phys. Lett.* **104**, 103108 (2014).
147. Dartiaillh, M.C., Kontos, T., Doucot, B. & Cottet, A. Direct Cavity Detection of Majorana Pairs. *Phys. Rev. Lett.* **118**, 126803 (2017).
148. Mourik, V. et al. Signatures of Majorana Fermions in Hybrid Superconductor-Semiconductor Nanowire Devices. *Science* **336**, 1003 (2012).
149. Albrecht, S.M. et al. Exponential protection of zero modes in Majorana islands. *Nature* **531**, 206 (2016).
150. Das, A. et al. Zero-bias peaks and splitting in an Al-InAs nanowire topological superconductor as a signature of Majorana fermions. *Nat. Phys.* **8**, 887 (2012).
151. Nadj-Perge, S. et al. Observation of Majorana fermions in ferromagnetic atomic chains on a superconductor. *Science* **346**, 602 (2014).
152. Trif, M. & Simon, P. Photon assisted braiding of Majorana fermions in a cavity. *arXiv:1810.00799* (2018).
153. Burkard, G. & Petta, J.R. Dispersive readout of valley splittings in cavity-coupled silicon quantum dots. *Phys. Rev. B* **94**, 195305 (2016).
154. Mi, X., Péterfalvi, C.G., Burkard, G. & Petta, J.R. High-Resolution Valley Spectroscopy of Si Quantum Dots. *Phys. Rev. Lett.* **119**, 176803 (2017).
155. Shim, Y., Ruskov, R., Hurst, H. & Tahan, C. Induced quantum dot probe for material characterization. *Appl. Phys. Lett.* **114**, 152105 (2019).
156. de Graaf, S.E., Danilov, A.V., Adamyan, A. & Kubatkin, S.E. A near-field scanning microwave microscope based on a superconducting resonator for low power measurements. *Rev. Sci. Instrum.* **84**, 023706 (2013).
157. Wang, J.I.J. et al. Coherent control of a hybrid superconducting circuit made with graphene-based van der Waals heterostructures. *Nat. Nanotechnol.* **14**, 120 (2019).
158. Goldhaber-Gordon, D. et al. Kondo effect in a single-electron transistor. *Nature* **391**, 156 (1998).

159. Goldhaber-Gordon, D. et al. From the Kondo regime to the mixed-valence regime in a single-electron transistor. *Phys. Rev. Lett.* **81**, 5225 (1998).
160. Desjardins, M.M. et al. Observation of the frozen charge of a Kondo resonance. *Nature* **545**, 71 (2017).
161. Hartke, T.R., Liu, Y.Y., Gullans, M.J. & Petta, J.R. Microwave Detection of Electron-Phonon Interactions in a Cavity-Coupled Double Quantum Dot. *Physical Review Letters* **120**, 097701 (2018).
162. Schneider, B.H., Etaki, S., van der Zant, H.S.J. & Steele, G.A. Coupling carbon nanotube mechanics to a superconducting circuit. *Sci. Rep.* **2**, 599 (2012).
163. Bockrath, M. et al. Luttinger-liquid behaviour in carbon nanotubes. *Nature* **397**, 598 (1999).
164. Jompol, Y. et al. Probing Spin-Charge Separation in a Tomonaga-Luttinger Liquid. *Science* **325**, 597 (2009).
165. Laroche, D., Gervais, G., Lilly, M.P. & Reno, J.L. 1D-1D Coulomb Drag Signature of a Luttinger Liquid. *Science* **343**, 631 (2014).
166. Wu, L. et al. Quantized Faraday and Kerr rotation and axion electrodynamics of a 3D topological insulator. *Science* **354**, 1124 (2016).